



Chemical looping reforming of the micromolecular component from biomass pyrolysis via Fe₂O₃@SBA-16

Yunchang Li¹ · Bo Zhang¹ · Xiantan Yang¹ · Bolun Yang¹ · Shengyong Zhang¹ · Zhiqiang Wu¹

Received: 26 May 2023 / Revised: 20 November 2023 / Accepted: 28 March 2024
© The Author(s) 2024

Abstract

To solve the problems of low gasification efficiency and high tar content caused by solid–solid contact between biomass and oxygen carrier in traditional biomass chemical looping gasification process. The decoupling strategy was adopted to decouple the biomass gasification process, and the composite oxygen carrier was prepared by embedding Fe₂O₃ in molecular sieve SBA-16 for the chemical looping reforming process of pyrolysis micromolecular model compound methane, which was expected to realize the directional reforming of pyrolysis volatiles to prepare hydrogen-rich syngas. Thermodynamic analysis of the reaction system was carried out based on the Gibbs free energy minimization method, and the reforming performance was evaluated by a fixed bed reactor, and the kinetic parameters were solved based on the gas–solid reaction model. Thermodynamic analysis verified the feasibility of the reaction and provided theoretical guidance for experimental design. The experimental results showed that the reaction performance of Fe₂O₃@SBA-16 was compared with that of pure Fe₂O₃ and Fe₂O₃@SBA-15, and the syngas yield was increased by 55.3% and 20.7% respectively, and it had good cycle stability. Kinetic analysis showed that the kinetic model changed from three-dimensional diffusion to first-order reaction with the increase of temperature. The activation energy was 192.79 kJ/mol by fitting. This paper provides basic data for the directional preparation of hydrogen-rich syngas from biomass and the design of oxygen carriers for pyrolysis of all-component chemical looping reforming.

Keywords Biomass pyrolysis · Methane · Chemical looping reforming · Oxygen carrier · Kinetic analysis

1 Introduction

Traditional fossil fuel is still the main energy material at present. With the rapid development of industry, fossil energy consumption is increasing, which accelerates the production of greenhouse gases and the depletion of non-renewable energy sources (Kierzkowska et al. 2013). Therefore, biomass has been widely studied as a green renewable energy application. As a new type of renewable energy, biomass has the advantages of extensive sources and environmental friendliness. Biomass gasification technology is the most

promising technology in biomass conversion applications. It can transform low-energy–density biomass into high-energy–density biogas, reducing the conditions and costs of transportation and storage and capturing CO₂ from the system (Zheng et al. 2021). And it can also be used to produce syngas used in industry to make downstream chemicals and as a fuel (Smolinski et al. 2022). In traditional biomass gasification, pyrolysis and reforming are coupled in the same reactor (Ding et al. 2022), and the reactions are numerous and complex which leads the lower syngas quality and higher tar content. Based on the above problems, chemical looping reforming based on the decoupling strategy is feasible (Zhang et al. 2023a, b; Liu et al. 2023). It can realize the high-efficiency conversion of biomass, improve the selectivity of syngas, and reduce system energy consumption, and has very important research value (Zhiqiang et al. 2019; Li et al. 2020; Luo et al. 2018; Tang et al. 2015).

Biomass chemical looping reforming is mainly aimed at reforming macromolecular and micromolecular volatiles. As shown in Fig. 1a, it is the traditional chemical looping

Yunchang Li and Bo Zhang are co-first author and contributes equally to this paper.

✉ Zhiqiang Wu
zhiqiang-wu@mail.xjtu.edu.cn

¹ Shaanxi Key Laboratory of Energy Chemical Process Intensification, School of Chemical Engineering and Technology, Xi'an Jiaotong University, Xi'an 710049, Shaanxi, People's Republic of China

gasification, oxygen carrier, and biomass are in the same reactor and the solid–solid reaction rate is low. As shown in Fig. 1b, it is the biomass chemical looping reforming based on a decoupling strategy. The gasification reactor is decoupled into pyrolysis and reforming reactors. The solid–solid reaction is also decomposed into several gas–solid reactions, which enhances the biomass gasification efficiency,

reduces the product's tar content, and targets the product distribution. Micromolecular gases react with lattice oxygen in metal oxides to undergo a partial oxidation reaction and generate hydrogen-rich syngas (Liu et al. 2019a). Currently, CH_4 is used as a model compound of micromolecular volatiles reforming process to study the chemical looping reforming reaction of micromolecular volatiles (Chuaiyboon

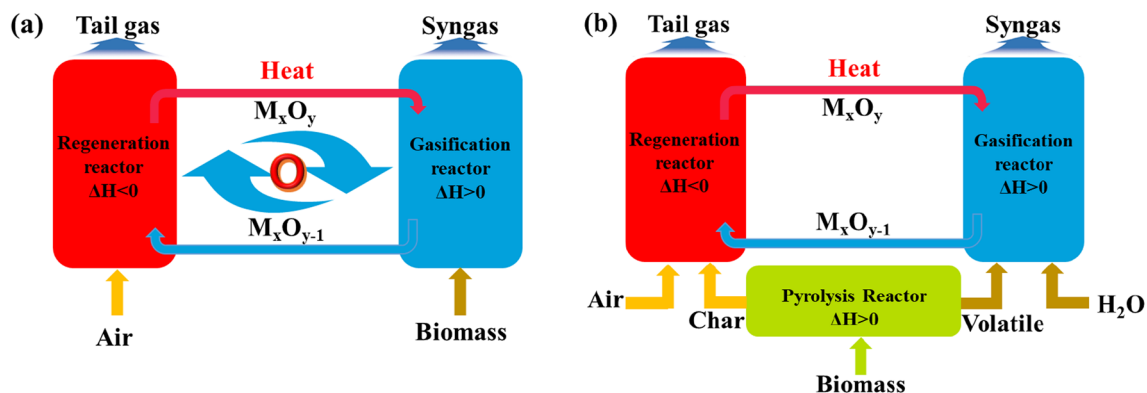


Fig. 1 a Traditional chemical looping gasification b Chemical looping reforming based on decoupling strategy

Table 1 Current study on chemical looping reforming methane

Organization	Oxygen carriers	Reaction conditions	Main conclusion
Kunming University of Science and Technology (Yang et al. 2021; Zhu et al. 2010)	La-Mn-Fe-O	700–800 °C Fixed bed reactor	The CH_4 conversion was more than 65%, the CO selectivity was more than 95%, and the H_2/CO was between 1.86 and 2.06. The oxygen carrier showed good stability during 10 cycles
	$\text{CeO}_2\text{-Fe}_2\text{O}_3$	850 °C Fixed bed reactor	CH_4 conversion could reach 50%, CO selectivity was close to 100%, and hydrogen carbon ratio was close to 2.0
Shiraz University (Alirezaei et al. 2016)	15Cu/20Zr-Al	550–750 °C Fixed bed reactor	$\text{CH}_4/\text{CO}_2 = 1$ and the reaction temperature of 750 °C. The highest methane conversion was 99.8%, and the highest CO_2 conversion was 99.2%. The activity did not decrease in 16 cycles
Qingdao Institute of Bioenergy and Bioprocess, CAS Technology (Ge et al. 2020)	V_2O_3	850 °C Fixed bed reactor	The highest CO selectivity was 99.5%, the H_2/CO ratio remained between 3.3 and 3.4, and the carbon deposition in 8 cycles was small
Dalian Institute of Chemical Physics, CAS (Kang et al. 2019)	$\text{Y-Fe}_2\text{O}_3/\text{Al}_2\text{O}_3$	850 °C Fixed bed reactor	With the addition of Y, the CO selectivity was up to 98%, and the conversion of CH_4 was up to 90%
Guangzhou Institute of Energy Conversion, CAS (Zhao et al. 2016, 2014)	$\text{LaFe}_{1-x}\text{Co}_x\text{O}_3$	850 °C Fixed bed reactor	CH_4 conversion was close to 85%, and H_2/CO was close to 2.0 in 20 cycles, but the selectivity of syngas was only 60%
	LaFeO_3	850 °C Fixed bed reactor	Within ten cycles, methane conversion fluctuated around 50%, CO selectivity was close to 100%, and H_2/CO was close to 6.0
Southeast University (Yin et al. 2020)	Fe@Ce	875 °C Fixed bed reactor	The maximum CH_4 conversion was about 50%, which decreased to about 30% after 16 cycles. The cycling performance was poor, and the selectivity was always maintained at 90%

et al. 2019; Kang et al. 2019; Liu et al. 2019b). As shown in Table 1, methane conversion, CO selectivity, H_2/CO , and cycle stability of oxygen carriers are all important indexes to measure the chemical looping reforming system of methane (Mao et al. 2022). It has shown that the research on chemical looping reforming is almost concentrated on the design of oxygen carriers such as metal oxygen carriers, composite metal oxygen carriers, core-shell structures, perovskite structures, etc. It has important guiding significance for the research of micromolecular chemical looping reforming.

Traditional single metal oxides were hard to have excellent comprehensive reaction performance simultaneously. For example, Ni-based oxygen carriers could achieve high CH_4 conversion but had low selectivity for partial oxidation (Zafar et al. 2005). Cu-based oxygen carriers had high oxygen storage capacity, but their melting point was low, agglomeration occurred at higher temperatures, and they had poor mechanical strength (Rydén et al. 2014). Fe-based oxygen carriers had good anti-aggregation ability and thermal stability, but reactivity was poor (Mattisson et al. 2001). Composite metal oxygen carriers, such as Ce-Fe, could improve the dispersion and enhance the interaction between metals by doping different metals (Li et al. 2011). Given the problems of low reactivity, poor mechanical strength, and easy sintering of traditional oxygen carriers, using the oxygen carriers embedding strategy is a novel means. Previous studies have reported that $Fe_2O_3@SBA-15$ was used for chemical looping reforming (Mao et al. 2022). SBA-15 has a two-dimensional pore structure in which Fe_2O_3 can be embedded to realize nano-scale and dispersive and enhance its reactivity. At the same time, under the protection of the molecular sieve cage structure, the anti-sintering ability can be improved to enhance recycling stability. However, from the perspective of microstructure, CH_4 is affected by the limited domain effect in two-dimensional channels (Du et al. 2021). The radial diffusion of gas molecules is blocked in the channel, which is not conducive to the reaction. Therefore, to mitigate the size effect by embedding Fe_2O_3 into the SBA-16 molecular sieve, which has a three-dimensional cubic mesoporous structure. Prof. Zhao's team synthesized SBA-16, an original cubic cage mesoporous structure with large cell parameters, using triblock copolymers (Zhao et al. 1998). There were few studies on the application of SBA-16, which was mainly applied to catalytic dry reforming of CH_4 (Mohan et al. 2013; Miaomiao et al. 2017; Zhang et al. 2013; Taherian et al. 2021), catalytic hydrogenation of CO (Budi et al. 2016; Chen et al. 2017). This paper proposes that Fe_2O_3 was embedded into SBA-16 molecular sieve, which had a three-dimensional ordered mesoporous structure. Based on this, the axial and radial diffusion resistance of CH_4 in the pore was greatly reduced. Compared with SBA-15, this limiting effect can be reduced to a certain degree,

thus strengthening diffusion of gas molecules and lattice oxygen and improving the reactivity of Fe_2O_3 .

In this paper, $Fe_2O_3@SBA-16$ was successfully prepared based on an embedding strategy. Methane was used as a model compound to study micromolecular chemical looping reforming. Reaction thermodynamics analysis of the chemical looping reforming system was implemented, and the influence of different Fe_2O_3 embedding ratios, CH_4 partial pressure, and reaction temperature for the reaction system was studied. The reaction performance of the $Fe_2O_3@SBA-16$ was compared with $Fe_2O_3@SBA-15$ and Fe_2O_3 . The cycling stability of $Fe_2O_3@SBA-16$ was tested through ten-cycle experiments, and the kinetic analysis of the oxygen carrier was implemented. The properties variation of $Fe_2O_3@SBA-16$ before and after the reaction was discussed.

2 Material and methods

2.1 Material preparation and characterization

2.1.1 Preparation of oxygen carriers

The molecular sieve was prepared by hydrothermal method in Fig. 2a. Polyethylene oxide-polypropylene oxide-polyethylene oxide (PEO-PO-PEO) block copolymers (0.50g P123, 2.51g F127) were mixed into 120 ml dilute hydrochloric acid solution according to appropriate proportion. After the solution was stirred at 35 °C for 6 h, a certain amount of tetraethyl orthosilicate (TEOS) was added for 15 min and then transferred to the hydrothermal reactor, where it was heated at 35 °C for 24 h and then at 100 °C for 24 h. Solid precursors were collected and dried in an oven at 100 °C for 12 h, then transferred to a Muffle furnace for 10 h calcination at 550 °C to obtain SBA-16 with a three-dimensional ordered mesoporous structure (Zhao et al. 1998).

As shown in Fig. 2b, $Fe_2O_3@SBA-16$ and $Fe_2O_3@SBA-15$ oxygen carrier was obtained by centrifugal immersion method. Weigh 50 ml ethanol solution and pour it into the beaker, add a certain amount of $Fe(NO_3)_3 \cdot 9H_2O$, stir for 15 min, then weigh a certain proportion of SBA-16 molecular sieve and put it into the beaker. Stir the mixture at room temperature for 12 h. Transfer the stirred solution to the centrifuge for centrifugal operation, pour out the supernatant, and dry in the oven for 2 h. Finally, the oxygen carrier $xFe_2O_3@SBA-16$ ($x = 10\%, 20\%, 30\%, 40\%$) was prepared by calcination in a muffle furnace at 600 °C for 5 h. The prepared oxygen carrier $xFe_2O_3@SBA-16$ was abbreviated as $xFe@S16$, and granulated to 40–60 meshes for subsequent use.



Fig. 2 a Preparation process of SBA-16 b Preparation process of $\text{Fe}_2\text{O}_3@\text{SBA-16}$

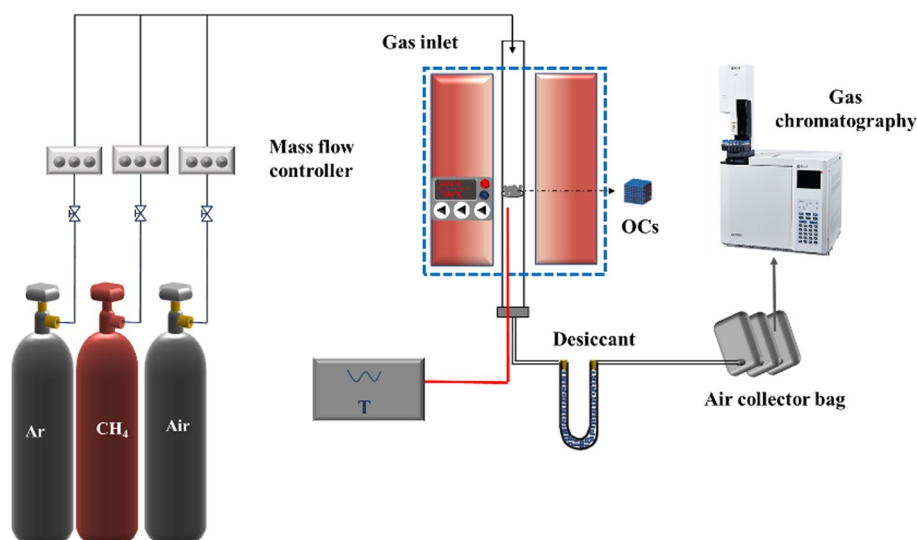
2.1.2 Characterization of oxygen carriers

$\text{Fe}_2\text{O}_3@\text{SBA-16}$ was characterized by an X-ray diffractometer (SHIMADZU XRD-6100) to analyze its XRD pattern and scanning 2θ angle range of 10° – 80° . Microstructure of the $\text{Fe}_2\text{O}_3@\text{SBA-16}$ was characterized by Field Emission Scanning Electron Microscope (FE-SEM, TESCAN MAIA3LMH) and Transmission Electron Microscope (TEM, JEM-2100Plus), and surface distribution of particles was characterized by Energy Dispersive Spectrometer (EDS). The specific surface area of SBA-16 and $\text{Fe}_2\text{O}_3@\text{SBA-16}$ and pore structure were characterized by automated surface area and porosity analyzer (BELSORP-Max).

2.2 Experimental setup

The performance of methane chemical looping reforming was tested in a fixed bed reactor using $x\%\text{Fe}_2\text{O}_3@\text{SBA-15/16}$. The experimental setup is shown in Fig. 3. The experimental device was mainly composed of a gas control system and a fixed bed reactor. The laboratory reactor was a quartz tube reactor with an inner diameter of 6 mm and a total length of 640 mm. The $\text{Fe}_2\text{O}_3@\text{SBA-16}/\text{Fe}_2\text{O}_3@\text{SBA-15}$ particles used in each experiment were 200 mg (40–60 mesh). At the beginning of the reaction, the Ar (100 mL/min) was first used to purge the pipeline for 30 min to eliminate the effect of air. The reactor

Fig. 3 Diagram of fixed bed experimental equipment



temperature was then increased to 800–950 °C at a heating rate of 10 °C/min. In the reaction stage, reaction gas (10%CH₄+90%Ar) was injected into the reactor for 5 min with a flow rate of 100 mL/min, in which Ar was the carrier gas. The reaction outlet gas was detected by gas chromatography (FULI 9790 II). In the regeneration stage, Ar (100 mL/min) purged the reactor for 30 min, and the oxygen carrier was regenerated by air (100 mL/min) for 15 min. After the regeneration reaction, Ar (100 mL/min) was injected repeat the above purging steps for the next cycle experiment.

2.3 Analytical method

CH₄ conversion, CO selectivity, H₂/CO ratio, lattice oxygen conversion of oxygen carriers, and gas concentration are calculated by the following formulas (Ding et al. 2019; Du et al. 2016):

$$\text{CH}_4 \text{ conversion} = \frac{\sum_{t_i}^{t_{i+1}} (n_{\text{CH}_4, \text{in}} - n_{\text{CH}_4, \text{out}})}{\sum_{t_i}^{t_{i+1}} n_{\text{CH}_4, \text{in}}} \times 100 \quad (1)$$

$$\text{CO selectivity} = \frac{\sum_{t_i}^{t_{i+1}} n_{\text{CO}}}{\sum_{t_i}^{t_{i+1}} (n_{\text{CO}} + n_{\text{CO}_2})} \times 100 \quad (2)$$

$$\text{H}_2/\text{CO} = \frac{\sum_{t_i}^{t_{i+1}} n_{\text{H}_2}}{\sum_{t_i}^{t_{i+1}} n_{\text{CO}}} \quad (3)$$

$$\text{Gas concentration} = \frac{V_i}{\sum V_i} \times 100 \quad (4)$$

$$[\text{O}] \text{ Conversion} = \frac{\sum_{t_i}^{t_{i+1}} n_{\text{CO}} + \sum_{t_i}^{t_{i+1}} n_{\text{CO}_2} \times 2}{n_{[\text{O}]_{\text{in}}}} \times 100 \quad (5)$$

where t_i, t_{i+1} is the initial reaction time, s; $n_{\text{CH}_4, \text{in}}$ is the amount of feed methane substance, mol; $n_{\text{CH}_4, \text{out}}$ is the amount of outlet methane substance, mol; $n_{\text{CO}}, n_{\text{CO}_2}$ are the content of carbon monoxide and carbon dioxide in outlet gas, mol; n_{H_2} is the amount of hydrogen substance in outlet gas, mol; V_i is the volume of substance i in outlet gas, ml; $n_{[\text{O}]_{\text{in}}}$ is the content of the total lattice oxygen substance in the feed oxygen carrier, mol.

2.3.1 Thermodynamic analysis method

In this experiment, thermodynamics analysis of the chemical looping reforming methane by minimum Gibbs free energy

Table 2 Fe₂O₃ may occur oxidation–reduction reaction in reforming reactor

Oxygen carrier	Reaction	No.
Fe ₂ O ₃	12Fe ₂ O ₃ + CH ₄ = 8Fe ₃ O ₄ + CO ₂ + 2H ₂ O	R1
	3Fe ₂ O ₃ + CH ₄ = 2Fe ₃ O ₄ + CO + 2H ₂	R2
	3Fe ₂ O ₃ + H ₂ = 2Fe ₃ O ₄ + H ₂ O	R3
	3Fe ₂ O ₃ + CO = 2Fe ₃ O ₄ + CO ₂	R4
Fe ₃ O ₄	4Fe ₃ O ₄ + CH ₄ = 12FeO + CO ₂ + 2H ₂ O	R5
	Fe ₃ O ₄ + CH ₄ = 3FeO + CO + 2H ₂	R6
FeO	4FeO + CH ₄ = 4Fe + CO ₂ + 2H ₂ O	R7
	FeO + CH ₄ = Fe + CO + 2H ₂	R8

method. After the ΔG of a reaction was solved, $\ln k$ could be solved according to $\Delta G = -RT \ln k$. Through thermodynamic analysis, it could prejudge the feasibility of the reaction. Table 2 lists 8 oxidation–reduction reactions that might occur during chemical looping reforming methane of Fe₂O₃. Thermodynamic behaviors of complete and partial oxidation of Fe₂O₃ were predicted.

2.3.2 Kinetic analysis method

The experiment results of Fe₂O₃ in methane chemical looping reforming were analyzed and discussed by the gas–solid reaction model, and the reaction mechanism was obtained. The kinetic parameters were determined by the following equations:

$$\frac{dX}{dt} = kf(X) \quad (6)$$

where X is lattice oxygen conversion, which is determined by the calculation of $[\text{O}]$ conversion in Eq. (5), k is the reaction rate constant, t is the reaction time, and $f(X)$ is the reaction mechanism function.

$$k = k_0 e^{\left(-\frac{E_a}{RT}\right)} \quad (7)$$

$$\ln k = -\frac{E_a}{R} \frac{1}{T} + \ln k_0 \quad (8)$$

where k_0 is the pre-exponential factor, E_a is the reaction activation energy, R is the gas constant, and T is the temperature.

Hancock and Sharp (Hancock 1972) proposed a method based on curve analysis to obtain the reaction mechanism by comparing the kinetic data of the experiment with the assumed kinetic data, as shown in Table 3, the experimental data can be used for correlation mapping in Eq. (9):

$$\ln[-\ln(1-X)] = m \ln(t) + \ln(n) \quad (9)$$

Table 3 The correspondence between the reaction mechanism model and m (Piotrowski et al. 2007; Provis 2016; Dollimore et al. 1996)

Reaction mechanism model	Differential formula $f(x) = \frac{1}{k} \frac{dx}{dt}$	Integral formula $g(x) = kt$	m
One-dimensional diffusion	$1/(2x)$	x^2	0.62
Two-dimensional diffusion	$-1/\ln(1-x)$	$x + (1-x)\ln(1-x)$	0.57
Three-dimensional diffusion	$[3(1-x)^{\frac{2}{3}}]/[2(1-(1-x)^{1/3})]$	$[1-(1-x)^{1/3}]^2$	0.54
First order reaction	$1-x$	$-\ln(1-x)$	1.00
Phase interface control	$3(1-x)^{2/3}$	$1-(1-x)^{1/3}$	1.07
Two-dimensional nuclear growth	$2(1-x)[- \ln(1-x)]^{1/2}$	$[- \ln(1-x)]^{1/2}$	2.00
Three-dimensional nuclear growth	$3(1-x)[- \ln(1-x)]^{2/3}$	$[- \ln(1-x)]^{1/3}$	3.00

where m is a constant related to the mechanism, and n is a constant related to the rate and frequency of grain growth.

3 Results and discussion

3.1 Thermodynamics analysis

For 8 reactions that might occur in the reaction system mentioned in Table 2, Fe_2O_3 may occur oxidation–reduction reaction in the reforming reactor the relationship between ΔG and $\log K$ of each reaction and the reaction temperature T was shown in Fig. 4. It was shown that when the reaction temperature was between 400 and 700 °C, the ΔG of the reaction R2 was less than 0, and the ΔG of the reaction R6 and R8 was greater than 0.

When the temperature was greater than 700 °C, the ΔG of the reaction R2, reaction R6, and reaction R8 was less than 0. From the perspective of thermodynamics analysis, at 400–700 °C, Fe_2O_3 could only be reduced to Fe_3O_4 stage, unable to release lattice oxygen fully. When the temperature exceeded 700 °C, the partial oxidation reaction (R2, R6, R8) between Fe_2O_3 and methane was thermodynamically feasible, and $\log K$ was greater than 0. The $\log K$ increased with increasing temperature, so it could be inferred that oxygen carriers in high-temperature regions are more likely to release lattice oxygen. The partial oxidation reaction Gibbs free energy of Fe_2O_3 with CH_4 (R2) was lower than that of FeO and the partial oxidation reaction of Fe_3O_4 with CH_4 (R6, R8). Fe_2O_3 was more easily reduced to FeO and Fe_3O_4 . Consistent results were obtained when H_2 was used as a reduction gas.

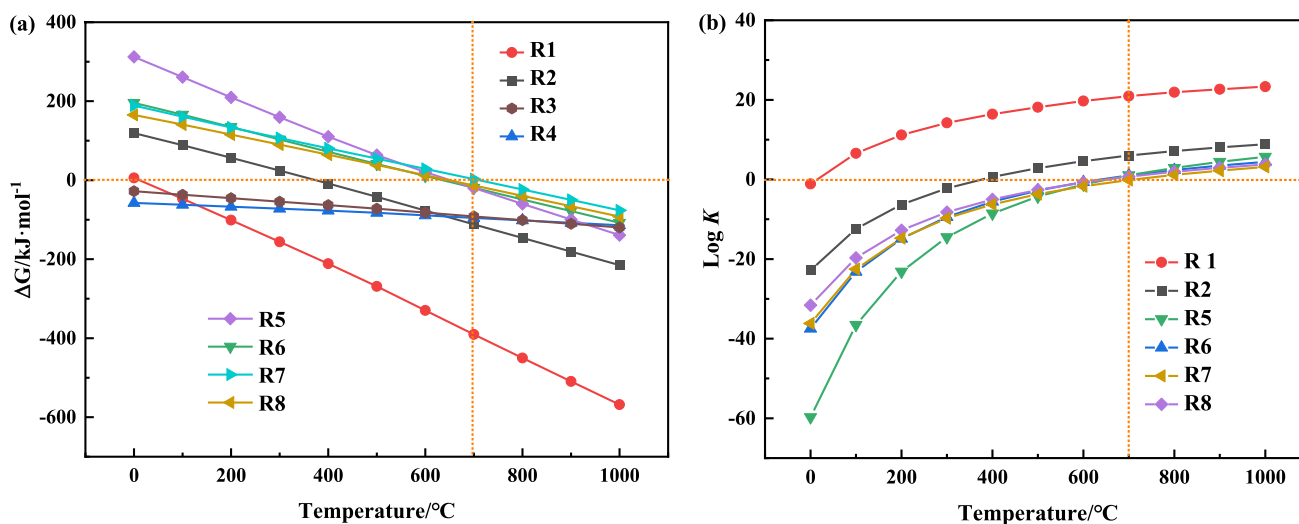


Fig. 4 The Gibbs free energy (ΔG) for 8 reactions and thermodynamic equilibrium constant ($\log K$) at the different reaction temperatures

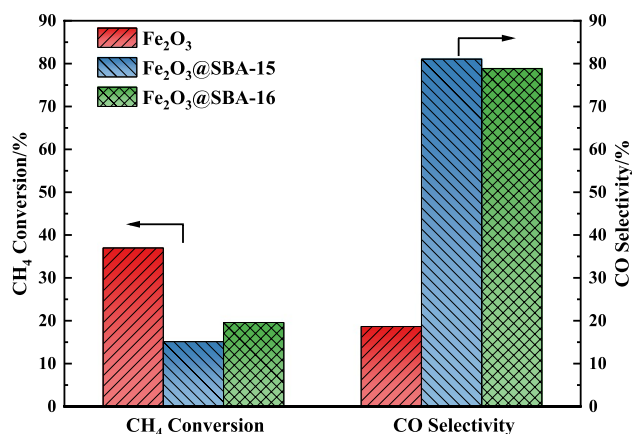


Fig. 5 Comparison of Fe₂O₃, Fe@S15, and Fe@S16 (900 °C, 0.8392 h⁻¹)

3.2 Analysis of chemical looping reforming methane of performance

3.2.1 Fe₂O₃@SBA-15/16 performance comparison

Fe₂O₃, Fe₂O₃@SBA-15 (Fe@S15), and Fe₂O₃@SBA-16 (Fe@S16) were compared under the same experimental conditions, and the differences in the performance of oxygen carriers embedded in different molecular sieves were discussed. As shown in Fig. 5, Pure Fe₂O₃ showed a higher CH₄ conversion rate of 35.6%, which was 100% and 80% higher than Fe@S15 (CH₄ conversion rate of 15.3%) and

Fe@S16 (CH₄ conversion rate of 19.8%), respectively. Regarding CO selectivity, pure Fe₂O₃ was only 18.6%, Fe@S16 (CO selectivity 79.1%) and Fe@S15 (CO selectivity 81.3%) increased nearly 400% compared with pure Fe₂O₃. It was attributed to the chemical looping reforming methane of pure Fe₂O₃, complete oxidation of methane dominated, resulting in a high CH₄ conversion rate and the reduction of CO in the product. The results showed that, compared with the embedding strategy of pure Fe₂O₃ and SBA-15, the partial oxidation activity of Fe@S16 was much higher than pure Fe₂O₃, and CH₄ conversion of Fe@S16 was nearly 30% higher than that of Fe@S15. In comparison, the CO selectivity of Fe@S16 was not decreased significantly (3%). It was shown that SBA-16 could enhance the reactivity of metal oxides compared with pure Fe₂O₃ and the SBA-15 embedding strategy. Oxygen carriers were embedded in SBA-15 of a two-dimensional ordered mesoporous structure (Zhang et al. 2022). The reaction performance was improved by realizing the nanocrystallization and dispersion of oxygen carrier particles. The size effect influenced methane, the micromolecule gas in SBA-15 pipeline could only diffuse in the axial direction of the channel, and the inner wall of the surrounding pipeline blocked the radial diffusion of the micromolecule. SBA-16 had a three-dimensional cubic ordered mesoporous structure (Kim et al. 2004), and its inner walls were all mesoporous pipelines. To some extent, it was beneficial to alleviate the influence of this size effect, thus promoting the diffusion of gas molecules and showing a better CO yield.

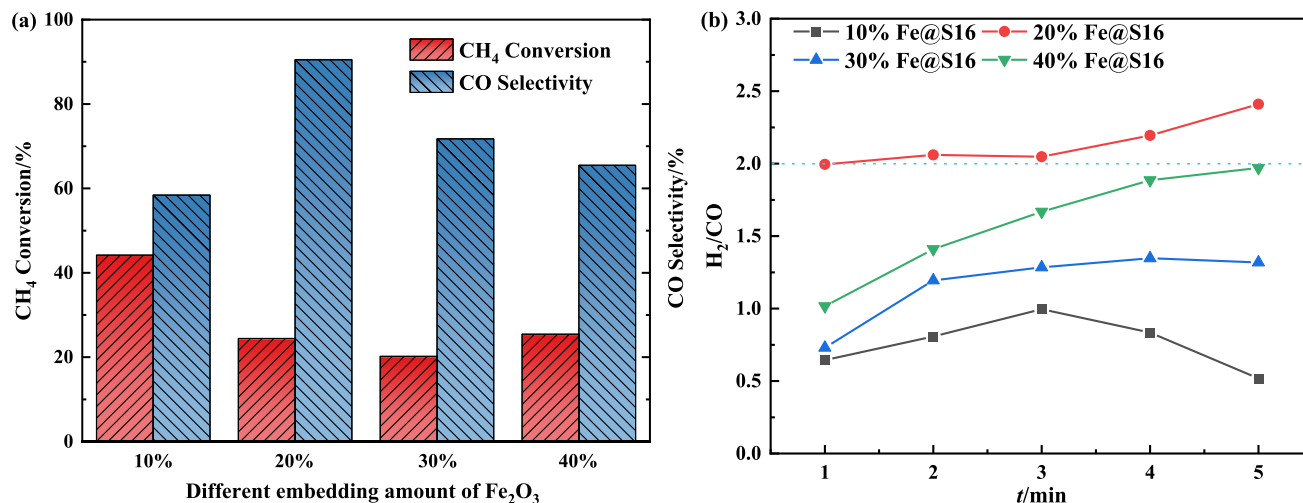


Fig. 6 Reactivity of different embedding quantities x Fe@S16 **a** CH₄ conversion and CO selectivity **b** Ratio of H₂/CO (900 °C, 0.8392 h⁻¹)

3.2.2 Effect of Fe₂O₃ embedding amount

Through the previous performance comparison, it could be concluded that Fe₂O₃@SBA-16 had more excellent performance in the chemical looping reforming of methane. Consequently, the influence of metal oxide embedding amount in Fe@S16 oxygen carrier was studied, and 10%Fe@S16, 20%Fe@S16, 30%Fe@S16, and 40%Fe@S16 were prepared, respectively. It could be seen in Fig. 6 that either too high or too low Fe embedding was not conducive to chemical looping reforming methane. With the Fe₂O₃ embedding amount increasing, the methane conversion rate showed an obvious decreasing trend. When the Fe₂O₃ embedding amount was 10%, the methane conversion rate was the highest and close to 40%, but the CO selectivity was poor at this

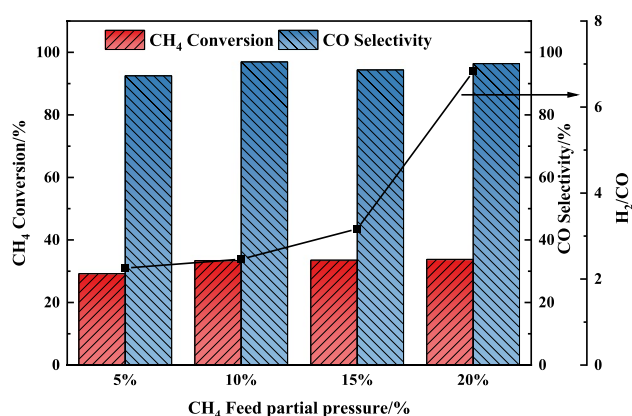


Fig. 7 Effect of different CH₄ feed partial pressure on reaction products (900 °C 0.8661 h⁻¹ (5%), 0.8392 h⁻¹ (10%), 0.8125 h⁻¹ (15%), 0.7857 h⁻¹ (20%))

time, only 58.4%. It was attributed to the fact that when Fe₂O₃ embedding was too low (10%), oxygen carriers on the molecular sieve surface and in the bulk phase were dispersed, resulting in sufficient gas–solid contact and leading to high methane conversion and low selectivity. The CO selectivity was raised first and then reduced with the growth of Fe₂O₃ embedding. When the Fe₂O₃ embedding amount was 20%, the CO selectivity reached the highest value of 90.5%. When Fe embedding was too high, oxygen carrier particles of the molecular sieve surface were unevenly distributed, which might aggravate the island effect of the solid product layer during the reaction process. The solid phase products continued to grow and cover the surface layer and the pores between the products. Once the continuous product layer was produced on the surface of Fe@S16 particles, the gas–solid contact would be seriously affected, thus affecting the diffusion of gas phase molecules and lattice oxygen. Therefore, CO selectivity was lower at higher oxygen carrier embedding. The result was a maximum selectivity of 90% at 20%Fe@S16 and an optimal H₂/CO ratio of 2.3, so the optimal Fe loading was 20%.

3.2.3 Effect of partial pressure on CH₄

In previous studies, we explored the influence of oxygen carrier embedding amount and obtained the optimal embedding amount of 20%. The content of methane in micromolecular volatile products of biomass pyrolysis usually ranges from 8% to 18% (Chang et al. 2016). Therefore, based on previous studies, the CH₄ feed partial pressure was changed (5%, 10%, 15%, 20%) in chemical looping reforming methane, and the effect of CH₄ feed partial pressure on the product was explored.

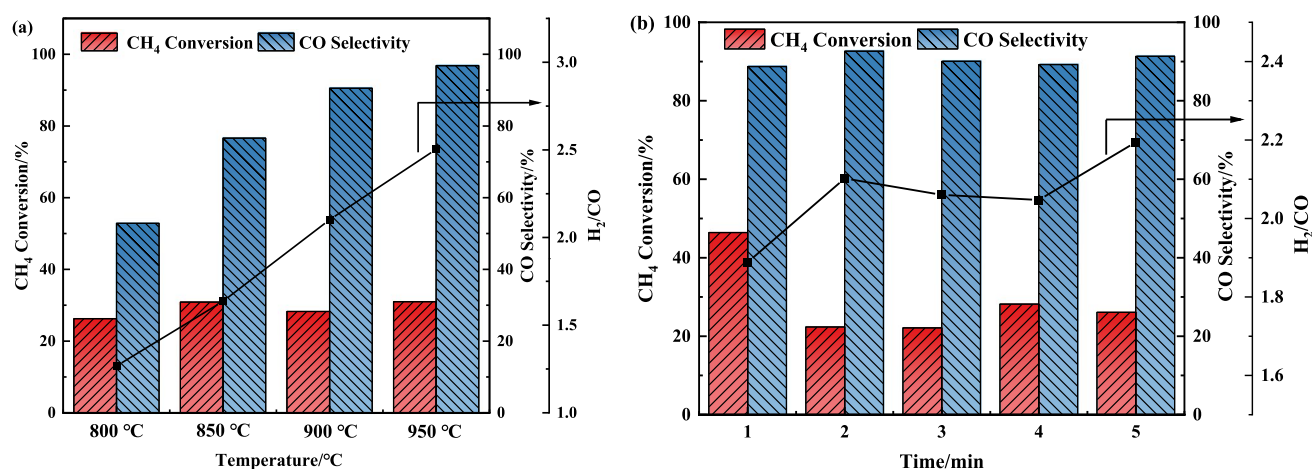


Fig. 8 a Influence of temperature on chemical looping reforming of methane, b 20%Fe@S16 real-time reactivity at 900 °C (10%CH₄, 0.8392 h⁻¹)

As shown in Fig. 7, when the partial pressure of methane increased from 5% to 10%, the CH_4 conversion increased to some extent. The highest CO selectivity of 96.81% and suitable H_2/CO (2.3) were obtained at 10% CH_4 partial pressure. The low feed partial pressure of methane led to poor CO selectivity, which was attributed to the preference of CH_4 to react with surface lattice oxygen and adsorbed oxygen (Cheng et al. 2016). Surface lattice oxygen and adsorption oxygen reaction activity were high so that the methane would be preferentially complete oxidation. It led to the increase of CO_2 content in the product and the decrease of CO selectivity. When CH_4 was higher than 10%, the CH_4 conversion and CO selectivity did not increase significantly and remained almost unchanged, but H_2/CO was unbalanced. It was attributed to the factor that in the high CH_4 feed partial pressure, and oxygen carriers could not provide sufficient lattice oxygen to react with methane. Methane cracking dominated and hydrogen production in the product increased, leading to the rise of H_2/CO . As a result, the high partial pressure of methane feed was not conducive to the partial oxidation of methane. Therefore, 10% was selected as the optimal partial pressure of CH_4 feed.

3.2.4 Effect of the reaction temperature

The effect of temperature on the chemical looping reforming of methane was studied based on the previously obtained 20% optimum embedding amount and 10% partial pressure of methane feed, as shown in Fig. 8a. With the reaction temperature rising, the selectivity of CO improved significantly in the range of 800–900 °C. The experiment result and the previous thermodynamic analysis were accordant. The

reaction temperature rise was beneficial to releasing lattice oxygen and partial methane oxidation. When the temperature exceeded 900 °C, the growth of CO selectivity was no longer obvious. At the same time, methane cracking increased significantly. The H_2/CO ratio was seriously unbalanced, and a large amount of carbon deposition was produced, which was not beneficial to the reaction. Hence the optimum reaction temperature was 900 °C. The methane conversion and CO selectivity during the reaction process at 900 °C were shown in Fig. 8b. In the first minute, the conversion of methane arrived at 40%. The lattice oxygen content in $\text{Fe}_2\text{O}_3@$ SBA-16 was adequate, and CH_4 reacted preferentially with the adsorbed oxygen on the oxygen carrier surface. Oxidation activities of adsorbed oxygen on the surface of oxygen carrier and surface lattice oxygen were greater than those of bulk lattice oxygen, resulting in high CH_4 conversion at the initial reaction stage. It could be seen that H_2/CO was only about 1.8 because part of H_2 was involved in complete oxidation, leading to H_2/CO being slightly lower than 2.0. After the first minute, most of the adsorbed oxygen and part of the surface lattice oxygen had been consumed, and oxygen vacancy was produced on the surface of the active component. The formation of surface oxygen vacancy was beneficial to partial methane oxidation (Cheng et al. 2016). It was shown that CH_4 conversion, CO selectivity, and the ratio of hydrogen to carbon monoxide remained basically stable in 2–4 min of reaction. At this moment, the lattice oxygen concentration gradient occurred between the interior of the bulk phase and the surface oxygen carrier (Zeng et al. 2018). As the bulk phase's lattice oxygen migrated to the surface, more oxygen vacancies were created inside the bulk phase. And the deeper lattice oxygen diffused to the outer layer reached

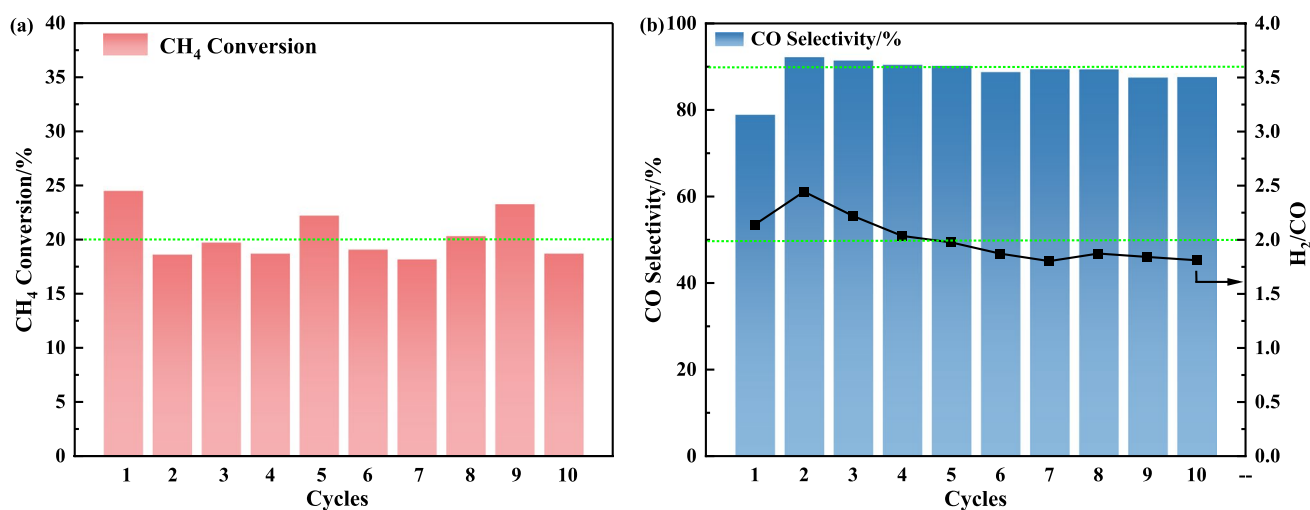


Fig. 9 20%Fe@S16 Ten-cycle performance **a** The CH_4 conversion **b** The CO selectivity and the ratio of H_2/CO (900 °C, 0.8392 h^{-1} , reaction time was 5 min, regeneration time was 15 min)

equilibrium over some time. When the reaction time reached the fifth minute, the lattice oxygen concentration of the bulk phase was too low, and the moving process of deeper lattice oxygen to the surface needed to overcome greater diffusion resistance. Meanwhile, CH₄ cracking was aggravated, and ratio of hydrogen to carbon monoxide was near to 2.5.

3.2.5 Cycle performance test

As shown in Fig. 9, ten cycle performance tests were conducted on 20%Fe@S16 oxygen carrier, and 20%Fe@S16 showed excellent cycle stability in the chemical looping reforming methane cycle test. In the first cycle, the selectivity of CO was only 80%, and the conversion of CH₄ was close to 25%. Because during the initial reaction, the surface lattice oxygen of 20%Fe@S16 was sufficient. It was beneficial to the complete oxidation of methane, resulting in a slightly lower selectivity of CO. From the second cycle, the CO selectivity could be stabilized at around 90%. In the tenth cycle experiment, the CO selectivity fluctuated by only 1% compared with the average selectivity of ten cycles (88.4%), and the CH₄ conversion fluctuated by only 1.3% compared with the average conversion of ten cycles (20.3%). H₂/CO could be maintained at around 2.0 during the ten cycles. In summary, 20%Fe@S16 oxygen carrier cycle stability was good. This might be because the Fe₂O₃ in the oxygen carrier improved its particles' specific surface area while realizing the nanocrystallization and could contact with oxygen more fully in the regeneration process. At the same time, the porous structure of the molecular sieve was also beneficial to the diffusion of gas and carbon deposition removal. Moreover, the SBA-16 porous molecular

Table 5 Physical parameters of oxygen carrier and molecular sieve

Samples	Pore size (nm)	Specific surface area (BET)/ (m ² /g)
SBA-16(This work)	3.3–3.5	720.9
SBA-16(Commercially available)	2.5–4.0	700
Fe ₂ O ₃ @SBA-16	2.34	757.25
Fe ₂ O ₃ @SBA-16(Used)	4.04	190.66
Fe ₂ O ₃ @SBA-16(Regeneration)	3.73	608.45

sieve framework had good structural stability at high temperatures, and the pore structure was not easy to collapse, which was conducive to improving the anti-sintering ability of Fe₂O₃@SBA-16.

As shown in Table 4, Both CeO₂-LaFeO₃ and Ce-Fe oxygen carriers could achieve high methane conversion, but the CO selectivity was only 40% and 79.7%, respectively. In the CeO₂-LaFeO₃ cycle experiment, the H₂/CO in the product ranged from 2 to 2.6, and the syngas quality was low. The selectivity of Ce-Fe was low, and the preparation of the oxygen carrier was relatively complicated. Fe₂O₃@CeO₂ maintained a high CO selectivity (95%) over 16 cycles, but the H₂/CO in the product was around 3.1, and the syngas quality was poor. The CO selectivity of LaFeO₃ only hovered between 55 and 75% in 10 cycles, and H₂/CO reached 2.5 to 3.1, which seriously affected the quality of syngas in the product. In this study, 20%Fe₂O₃@SBA-16 not only maintained high CO selectivity (90%) during ten-cycle experiments but also maintained H₂/CO in the product near 2.0, and the syngas quality in the product was very high.

Table 4 Comparison of oxygen carrier cycle reactivity

Oxygen carrier	Reaction conditions	CH ₄ Conversion	CO Selectivity	H ₂ /CO	Number of cycles	Organization
CeO ₂ /LaFeO ₃	850 °C Fixed-bed 40% CH ₄	65%	40%	2–2.6	10	Nanjing University of Science and Technology (Fang et al. 2021)
Ce-Fe	850 °C Fixed-bed 10% CH ₄	90.9%	79.7%	2.06	10	Institute of Coal Chemistry, CAS (Zhang et al. 2014)
Fe ₂ O ₃ @CeO ₂	875 °C Fixed-bed 7% CH ₄	~17%	~95%	~3.1	16	Southeast University (Yin et al. 2020)
LaFeO ₃	850 °C Fixed-bed 40% CH ₄	35–50%	55–75%	2.5–3.1	10	Guangzhou Institute of Energy Conversion, CAS (Zhao et al. 2014)
Fe ₂ O ₃ @SBA-16	900 °C Fixed-bed 10% CH ₄	~20.3%	90.0%	2.0	10	This work

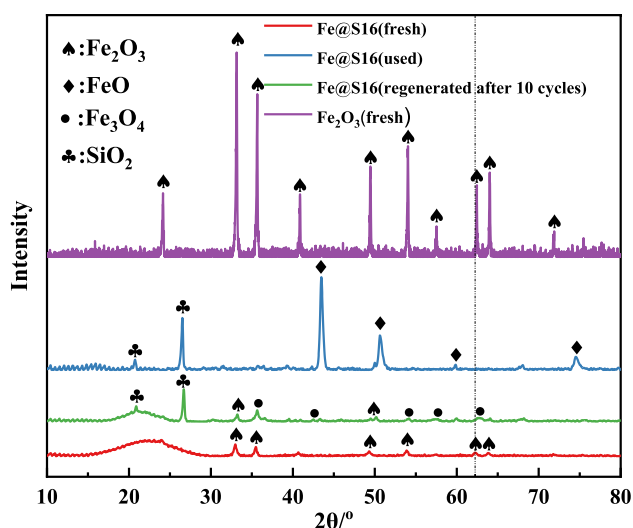


Fig. 10 XRD pattern of different oxygen carriers

3.3 Characterization of oxygen carriers

As shown in Table 5, the specific surface area ($720.9 \text{ m}^2/\text{g}$) and pore size parameters ($3.3\text{--}3.5 \text{ nm}$) of SBA-16 prepared in this experiment were the same as that of commercial SBA-16 molecular sieve ($700 \text{ m}^2/\text{g}$) and pore size parameters ($2.5\text{--}4.0 \text{ nm}$). The specific surface area of $\text{Fe}_2\text{O}_3@$ SBA-16 was slightly increased compared to SBA-16. However, the pore size remained almost unchanged, and the pore structure of the molecular sieve was maintained well. Therefore, Fe_2O_3 embedding was realized without changing the framework structure of the molecular sieve. After 10 cycles of the oxygen carrier, the specific surface area was seriously attenuated. The sintering of the oxygen carrier may be part of the reason for the attenuation of the specific surface area, but the carbon deposition on the specific surface of the oxygen carrier after the reaction seriously also affected the specific surface area. The specific surface area was $608.45 \text{ m}^2/\text{g}$ after cyclic regeneration, which basically recovered.

Wide-angle XRD characterization tests were conducted on the fresh $20\%\text{Fe}@$ S16, used $20\%\text{Fe}@$ S16, and regenerated after 10 cycles of $20\%\text{Fe}@$ S16, respectively. As shown in Fig. 10, the characteristic peaks of Fe_2O_3 were observed in fresh oxygen carriers. The XRD pattern of the used oxygen carrier showed an obvious FeO characteristic diffraction peak, which accorded with the previous thermodynamic analysis results. CH_4 was more likely to reduce Fe_2O_3 to FeO, so there would be a large amount of FeO. After ten cycles of regeneration, the XRD spectra showed obvious characteristic diffraction peaks of Fe_3O_4 and Fe_2O_3 . The characteristic peaks of Fe_3O_4 in the XRD pattern

showed that the oxygen carrier was not fully oxidized after ten cycles. This was due to the short regeneration time of $\text{Fe}_2\text{O}_3@$ SBA-16 and the slight sintering that occurred on the surface of $\text{Fe}_2\text{O}_3@$ SBA-16 after ten cycles, which affected sufficient contact between gas and solid, resulting in an inadequate reaction.

As shown in Fig. 11, the fresh $20\%\text{Fe}_2\text{O}_3@$ SBA-16, used $20\%\text{Fe}_2\text{O}_3@$ SBA-16 and regenerated after 10 cycles $20\%\text{Fe}_2\text{O}_3@$ SBA-16 were scanned by SEM and TEM in high-resolution mode. It could be seen from the comparison of Fig. 11a, c. After ten cycles, the surface of the used $\text{Fe}_2\text{O}_3@$ SBA-16 was partially sintering compared with the fresh $\text{Fe}_2\text{O}_3@$ SBA-16, forming a massive irregular structure of $2\text{--}3 \mu\text{m}$. It made the gas–solid contact on the surface of the oxygen carrier more difficult and required a longer reaction time to replenish lattice oxygen completely. The morphology of the used oxygen carrier changed obviously, as shown in Fig. 11b, but the spherical particle morphology could still be recovered after regeneration. The TEM images of the $20\%\text{Fe}@$ S16 in Fig. 11d, e showed that Fe_2O_3 nanoparticles were spherical and dispersed in highly ordered SBA-16 three-dimensional interconnecting channels. As shown in Fig. 11f, the response signal of an iron element in the EDS spectrum was evenly distributed, which further indicated that Fe_2O_3 was evenly dispersed. The TEM images of the used oxygen carrier Fig. 11g, h showed that the structure of the molecular sieve was still maintained, which verified the stability of the structure.

3.4 Kinetic analysis

In terms of the kinetic calculation model listed in Sect. 2.3.2 and real-time conversion data of lattice oxygen obtained from the experiment, the $20\%\text{Fe}@$ S16 reaction kinetic data was obtained. As shown in Fig. 12a, in terms of lattice oxygen conversion X , the m value was obtained by fitting. The corresponding reaction mechanism equation was decided by fitting the experiment data, and reaction rate constant k was obtained, as shown in Fig. 12b. The activation energy was obtained by fitting $\ln(k)$ and T , as shown in Fig. 12c. The final results are shown in Table 6.

Different reaction mechanism models were selected by referring to m values at different temperatures. At $750\text{--}850 \text{ }^\circ\text{C}$, the three-dimensional diffusion model was more suitable for fitting. At higher temperatures, the reaction was first order controlled at $850\text{--}950 \text{ }^\circ\text{C}$. At lower temperatures, the reaction of chemical looping reforming was mainly controlled by the diffusion step, which meant that diffusion of lattice oxygen was the main rate-limiting step. With increasing temperature, the reaction in a high-temperature region transferred to the first-order reaction,

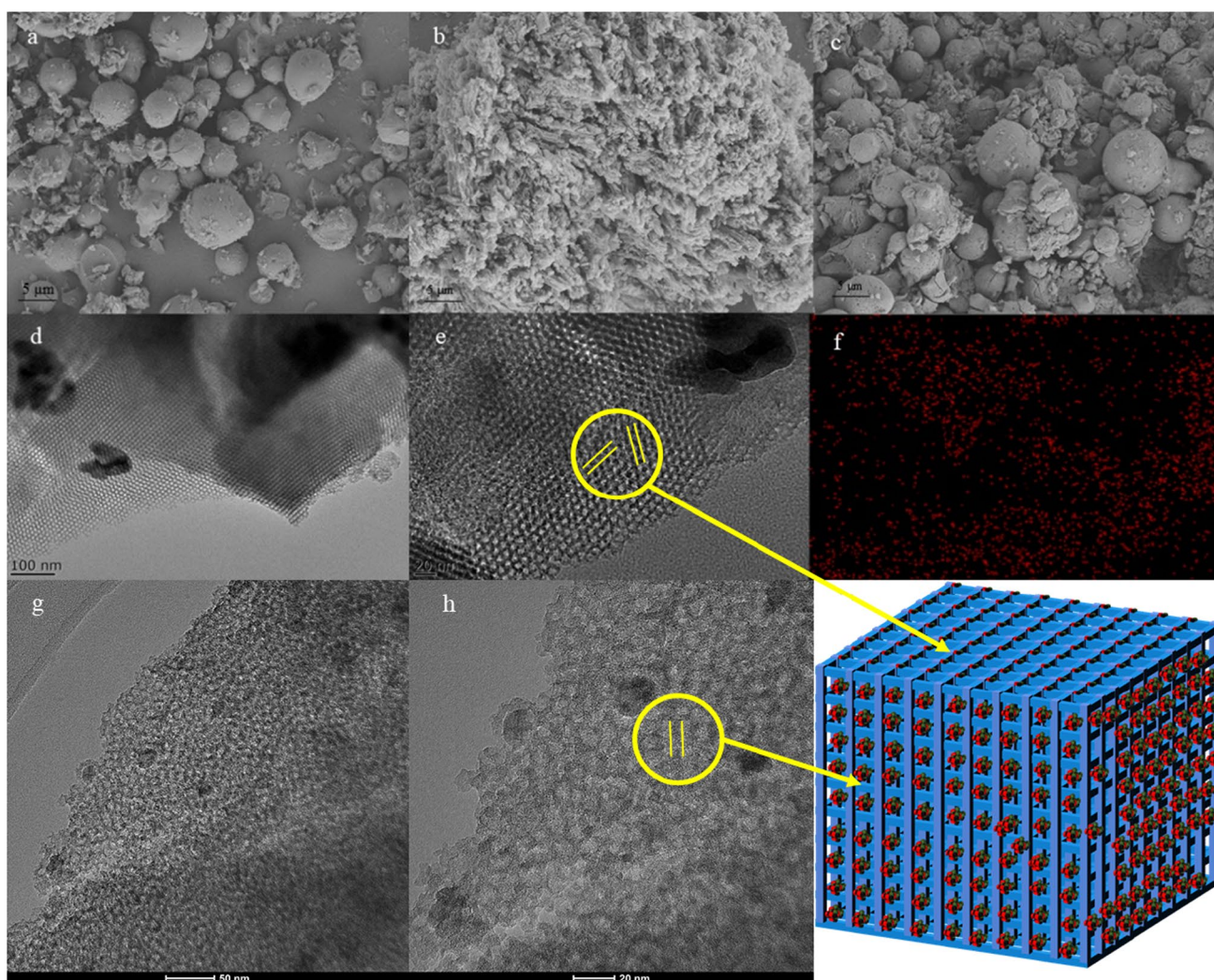


Fig. 11 20%Fe@SBA-16 **a** SEM image of the fresh 20%Fe@S16 **b** SEM image of the used 20%Fe@S16 **c** SEM image of 20%Fe@S16 after ten cycles of regeneration **d**, **e** TEM images of the fresh 20%Fe@S16 **f** EDS of 20%Fe@S16 **g**, **h** TEM images of the used 20%Fe@S16

and molecular diffusion was no longer the main rate-limiting step. Chemical looping reforming methane activation energy was 192.79 kJ/mol by fitting experiment data, consistent with the activation energy reported in current studies (Go et al. 2008; Hosseini et al. 2020).

4 Conclusions

In this paper, the characteristics of chemical looping reforming of micromolecular methane from biomass pyrolysis based on a decoupling strategy were studied. The composite oxygen carrier Fe_2O_3 @SBA-16 prepared by molecular sieve embedding strategy improved the

reaction performance. Compared with Fe_2O_3 and Fe_2O_3 @SBA-15, the yield of CO increased by 77.63% and 26.03% respectively when using Fe_2O_3 @SBA-16, in which the conversion of CH_4 reached 30.9% and the selectivity of CO reached 96.2%. In the ten-cycle experiments under the optimal reaction conditions, the CH_4 conversion and CO selectivity fluctuated within 2%. It was proved that Fe_2O_3 @SBA-16 had good cycle stability and sintering resistance. The kinetic model of the reaction was a three-dimensional diffusion control model and first-order reaction control model through kinetic data fitting, and the activation energy of the reaction was 192.79 kJ/mol. This work provides a certain experimental and research basis for the study of the chemical looping reforming process of biomass and the design of oxygen carrier.

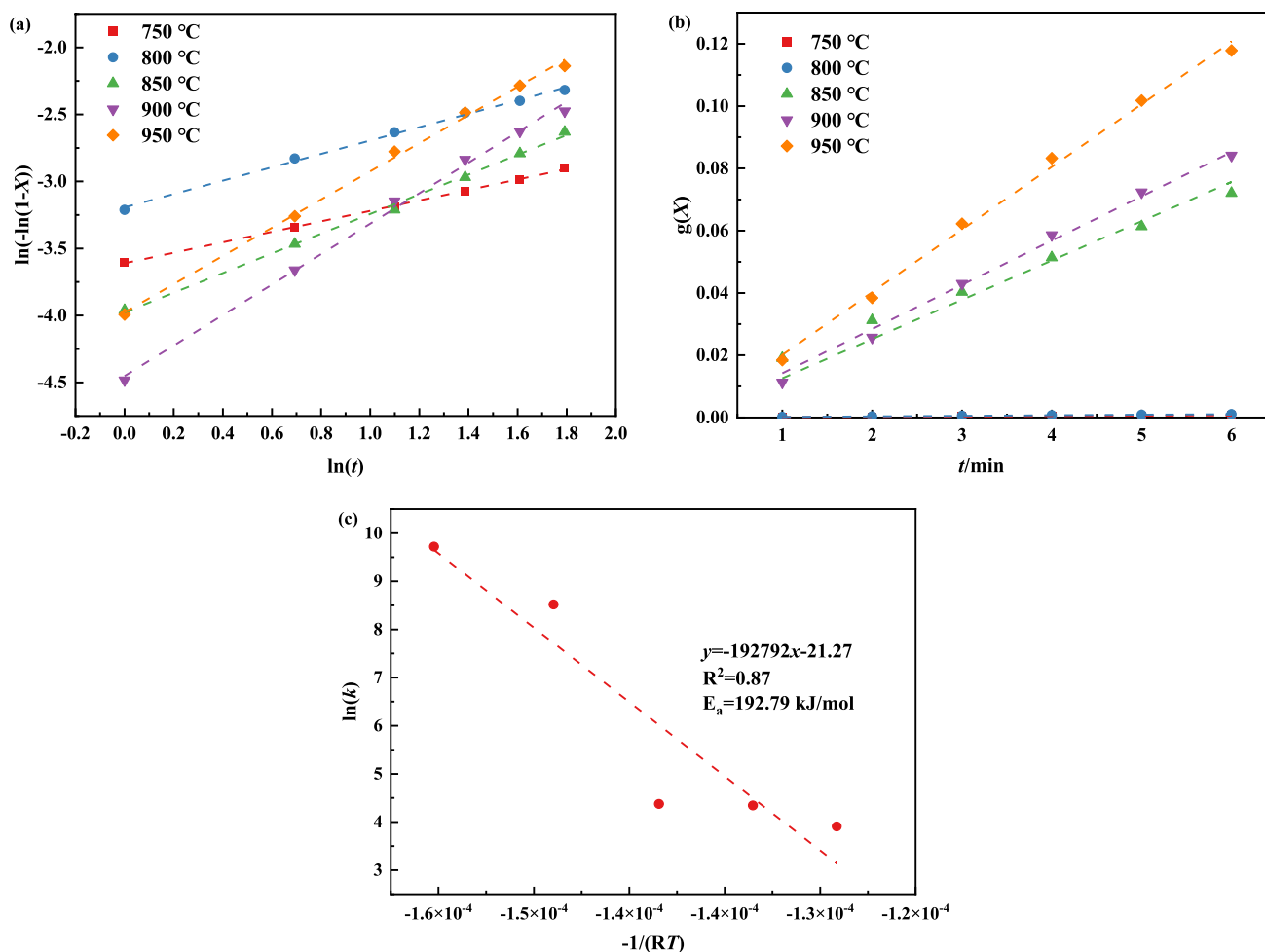


Fig. 12 Fitting of kinetic data **a** fitting of m **b** fitting of k **c** fitting of E

Table 6 Reaction kinetics calculation and fitting results

Tem- perature (°C)	m	R^2	$\ln k$	R^2	Reaction mechanism
750	0.391	0.999	9.721	0.950	Three-dimensional diffusion
800	0.504	0.997	8.517	0.995	Three-dimensional diffusion
850	0.738	0.997	4.374	0.948	First order reaction
900	1.141	0.997	4.343	0.994	First order reaction
950	1.051	0.998	3.907	0.996	First order reaction

Acknowledgements The authors gratefully acknowledge the support of the National Natural Science Foundation of China (Grant Nos: 22038011, 51976168), the K. C. Wong Education Foundation, the Natural Science Basic Research Program of Shaanxi (Program No. 2021JLM-17), the Programme of Introducing Talents of Discipline to Universities (B23025), and Innovation Capability Support Program of Shaanxi (Program Nos: 2023KJXX-004, 2023-CX-TD-26, 2022KXJ-126).

Author contributions YL: Conceptualization, Methodology, Data Curation, Writing—original draft. BZ: Conceptualization, Methodology, Data Curation, Writing—original draft. XY: Investigation, Visualization. BY: Funding acquisition, Supervision. SZ: Project administration, Supervision. ZW: Writing - Review & Editing, Funding acquisition.

Declarations

Competing interests The authors declare that they have no competing interests.

Open Access This article is licensed under a Creative Commons Attribution 4.0 International License, which permits use, sharing, adaptation, distribution and reproduction in any medium or format, as long as you give appropriate credit to the original author(s) and the source, provide a link to the Creative Commons licence, and indicate if changes were made. The images or other third party material in this article are included in the article's Creative Commons licence, unless indicated otherwise in a credit line to the material. If material is not included in the article's Creative Commons licence and your intended use is not permitted by statutory regulation or exceeds the permitted use, you will

need to obtain permission directly from the copyright holder. To view a copy of this licence, visit <http://creativecommons.org/licenses/by/4.0/>.

References

- Alirezai I, Hafizi A, Rahimpour MR, et al. Application of zirconium modified Cu-based oxygen carrier in chemical looping reforming. *J CO₂ Util* 2016;14:112–121.
- Budi CS, Wu HC, Chen CS et al (2016) Ni nanoparticles supported on cage-type mesoporous silica for CO₂ hydrogenation with high CH₄ selectivity. *ChemSusChem* 9(17):2326–2331
- Chang G, Huang Y, Xie J et al (2016) The lignin pyrolysis composition and pyrolysis products of palm kernel shell, wheat straw, and pine sawdust. *Energy Convers Manag* 124:587–597
- Chen C-S, Budi CS, Wu H-C et al (2017) Size-tunable Ni nanoparticles supported on surface-modified, cage-type mesoporous silica as highly active catalysts for CO₂ hydrogenation. *ACS Catal* 7(12):8367–8381
- Cheng Z, Qin L, Guo M et al (2016) Oxygen vacancy promoted methane partial oxidation over iron oxide oxygen carriers in the chemical looping process. *Phys Chem Chem Phys* 18(47):32418–32428
- Chuayboon S, Abanades S, Rodat S (2019) Syngas production via solar-driven chemical looping methane reforming from redox cycling of ceria porous foam in a volumetric solar reactor. *Chem Eng J* 356:756–770
- Ding H, Luo C, Li X et al (2019) Development of BaSrCo-based perovskite for chemical-looping steam methane reforming: a study on synergistic effects of A-site elements and CeO₂ support. *Fuel* 253:311–319
- Ding L, Yang M, Dong K et al (2022) Mobile power generation system based on biomass gasification. *Int J Coal Sci Technol* 9(1):34
- Dollimore D, Tong P, Alexander KS (1996) The kinetic interpretation of the decomposition of calcium carbonate by use of relationships other than the Arrhenius equation. *Thermochim Acta* 283:13–27
- Du Y, Zhu X, Wang H et al (2016) Synthesis gas generation by chemical-looping selective oxidation of methane using Pr_{1-x}Zr_xO_{2-δ} oxygen carriers. *J Energy Inst* 89(4):745–754
- Du Y, Fang X, Zhang T (2021) Confinement effect in zeolite catalysts. *Scientia Sinica Chimica* 51(2):87–96
- Fang X, Zhao K, Zhao Z et al (2021) Study of CeO₂/LaFeO₃ in chemical looping reforming of methane for syngas production. *J Fuel Chem Technol* 49(09):1250–1260
- Ge YZ, He T, Wang ZQ et al (2020) Chemical looping oxidation of CH₄ with 99.5% CO selectivity over V₂O₃-based redox materials using CO₂ for regeneration. *AIChE J* 66(1):10
- Go K, Son S, Kim S (2008) Reaction kinetics of reduction and oxidation of metal oxides for hydrogen production. *Int J Hydrogen Energy* 33(21):5986–5995
- Hancock JD (1972) Method of comparing solid-state kinetic data and its application to the decomposition of kaolinite, brucite, an BaCO₃. *J Am Ceram Soc* 55:74–77
- Hosseini SY, Khosravi-Nikou MR, Shariati A (2020) Kinetic study of the reduction step for chemical looping steam methane reforming by CeO₂-Fe₂O₃ oxygen carriers. *Chem Eng Technol* 43(3):540–552
- Kang Y, Tian M, Huang C et al (2019) Improving syngas selectivity of Fe₂O₃/Al₂O₃ with yttrium modification in chemical looping methane conversion. *ACS Catal* 9(9):8373–8382
- Kierzkowska AM, Poulidakos LV, Broda M et al (2013) Synthesis of calcium-based, Al₂O₃-stabilized sorbents for CO₂ capture using a co-precipitation technique. *Int J Greenhouse Gas Control* 15:48–54
- Kim TW, Ryoo R, Kruk M et al (2004) Tailoring the pore structure of SBA-16 silica molecular sieve through the use of copolymer blends and control of synthesis temperature and time. *J Phys Chem B* 108(31):11480–11489
- Li K, Wang H, Wei Y et al (2011) Partial oxidation of methane to syngas with air by lattice oxygen transfer over ZrO₂-modified Ce-Fe mixed oxides. *Chem Eng J* 173(2):574–582
- Li D, Xu R, Li X et al (2020) Chemical looping conversion of gaseous and liquid fuels for chemical production: a review. *Energy Fuels* 34(5):5381–5413
- Liu G, Liao Y, Wu Y et al (2019a) Enhancement of Ca₂Fe₂O₅ oxygen carrier through Mg/Al/Zn oxide support for biomass chemical looping gasification. *Energy Convers Manag* 195:262–273
- Liu Y, Qin L, Cheng Z et al (2019b) Near 100% CO selectivity in nanoscaled iron-based oxygen carriers for chemical looping methane partial oxidation. *Nat Commun* 10(1):5503
- Liu G, Zhang R, Zhang B et al (2023) Performance evaluation of torrefaction coupled with a chemical looping gasification process under autothermal conditions: flexible syngas production from biomass. *Energy Fuels* 37(1):424–438
- Luo M, Yi Y, Wang S et al (2018) Review of hydrogen production using chemical-looping technology. *Renew Sustain Energy Rev* 81:3186–3214
- Mao X, Liu G, Yang B et al (2022) Chemical looping reforming of toluene via Fe₂O₃@SBA-15 based on controlling reaction micro-environments. *Fuel* 326:125024
- Mattisson T, Lyngfelt A, Cho P (2001) The use of iron oxide as an oxygen carrier in chemical-looping combustion of methane with inherent separation of CO₂. *Fuel* 80(13):1953–1962
- Miaomiao H, Lin L, Xin Z et al (2017) Synthesis of Ni-based catalysts supported on nitrogen-incorporated SBA-16 and their catalytic performance in the reforming of methane with carbon dioxide. *J Fuel Chem Technol* 45(02):172–181
- Mohan N, Xiaojuan F, Yanqiu L et al (2013) Catalytic performance of mesoporous material supported bimetallic carbide Ni-β-Mo₂C/SBA-16 catalyst for CH₄/CO₂ reforming to syngas. *Chin J Catal* 34(02):379–384
- Piotrowski K, Mondal K, Wiltowski T et al (2007) Topochemical approach of kinetics of the reduction of hematite to wüstite. *Chem Eng J* 131(1–3):73–82
- Provis JL (2016) On the use of the Jander equation in cement hydration modelling. *RILEM Tech Lett* 1:62–66
- Rydén M, Jing D, Källén M et al (2014) CuO-based oxygen-carrier particles for chemical-looping with oxygen uncoupling—experiments in batch reactor and in continuous operation. *Ind Eng Chem Res* 53(15):6255–67
- Smolinski A, Wochna S, Howaniec N (2022) Gasification of lignite from Polish coal mine to hydrogen-rich gas. *Int J Coal Sci Technol* 9(1):77
- Taherian Z, Khataee A, Orooji Y (2021) Nickel-based nanocatalysts promoted over MgO-modified SBA-16 for dry reforming of methane for syngas production: impact of support and promoters. *J Energy Inst* 97:100–108
- Tang M, Xu L, Fan M (2015) Progress in oxygen carrier development of methane-based chemical-looping reforming: a review. *Appl Energy* 151:143–156
- Yang Z, Zheng Y, Li K et al (2021) Chemical-looping reforming of methane over La-Mn-Fe-O oxygen carriers: Effect of calcination temperature. *Chem Eng Sci* 229:116085
- Yin X, Wang S, Sun R et al (2020) A Ce-Fe oxygen carrier with a core-shell structure for chemical looping steam methane reforming. *Ind Eng Chem Res* 59(21):9775–9786
- Zafar Q, Mattisson T, Gevert B (2005) Integrated hydrogen and power production with CO₂ capture using chemical-looping reforming redox reactivity of particles of CuO, Mn₂O₃, NiO, and Fe₂O₃ using SiO₂ as a support. *Ind Eng Chem Res* 44(10):3485–3496

- Zeng L, Cheng Z, Fan JA et al (2018) Metal oxide redox chemistry for chemical looping processes. *Nat Rev Chem* 2(11):349–364
- Zhang SH, Muratsugu S, Ishiguro N et al (2013) Ceria-doped Ni/SBA-16 catalysts for dry reforming of methane. *ACS Catal* 3(8):1855–1864
- Zhang J, Jiejie H, Yitian F et al (2014) Partial oxidation reforming of methane to synthesis gas by chemical-looping using CeO₂-modified Fe₂O₃ as oxygen carrier. *J Fuel Chem Technol* 42(02):158–165
- Zhang B, Li Y, Yang B et al (2022) Controlling the reaction microenvironments through an embedding strategy to strengthen the chemical looping reforming of methane based on decoupling process. *Chem Eng J* 446:137061
- Zhang R, Guo W, Sun Z et al (2023) Effects of oxidative torrefaction conditions on the biomass liquid chemical looping reaction from the perspective of thermal behavior and kinetic analysis. *Fuel* 331:125924
- Zhang B, Sun Z, Li Y et al (2023b) Chemical looping reforming characteristics of methane and toluene from biomass pyrolysis volatiles based on decoupling strategy: embedding NiFe₂O₄ in SBA-15 as an oxygen carrier. *Chem Eng J* 466:143228
- Zhao DY, Huo QS, Feng JL et al (1998) Nonionic triblock and star diblock copolymer and oligomeric surfactant syntheses of highly ordered, hydrothermally stable, mesoporous silica structures. *J Am Chem Soc* 120(24):6024–6036
- Zhao K, He F, Huang Z et al (2014) Three-dimensionally ordered macroporous LaFeO₃ perovskites for chemical-looping steam reforming of methane. *Int J Hydrogen Energy* 39(7):3243–3252
- Zhao K, He F, Huang Z et al (2016) Perovskite-type oxides LaFe_{1-x}CoO₃ for chemical looping steam methane reforming to syngas and hydrogen co-production. *Appl Energy* 168:193–203
- Zheng S, Shi Y, Wang Z et al (2021) Development of new technology for coal gasification purification and research on the formation mechanism of pollutants. *Int J Coal Sci Technol* 8(3):335–348
- Zhiqiang W, Bo Z, Bolun Y (2019) Research progress on biomass chemical-looping conversion technology. *CIESC J* 70(08):2835–2853
- Zhu X, Wang H, Wei Y et al (2010) Hydrogen and syngas production from two-step steam reforming of methane over CeO₂-Fe₂O₃ oxygen carrier. *J Rare Earths* 28(6):907–913

Publisher's Note Springer Nature remains neutral with regard to jurisdictional claims in published maps and institutional affiliations.